

On the role of interfacial stabilization in the Rayleigh-Bénard convection of liquid-liquid dispersions

Francesca Pelusi,^{1,*} Andrea Scagliarini,^{2,3} Mauro Sbragaglia,⁴ Massimo Bernaschi,² and Roberto Benzi^{5,4}

¹*Istituto per le Applicazioni del Calcolo, CNR - Via Pietro Castellino 111, 80131 Naples, Italy*

²*Istituto per le Applicazioni del Calcolo, CNR - Via dei Taurini 19, 00185 Rome, Italy*

³*INFN, Sezione Roma “Tor Vergata”, Via della Ricerca Scientifica 1, 00133 Rome, Italy*

⁴*Department of Physics & INFN, Tor Vergata University of Rome,
Via della Ricerca Scientifica 1, 00133 Rome, Italy*

⁵*Sino-Europe Complex Science Center, School of Mathematics
North University of China, Shanxi, Taiyuan 030051, China*

(Dated: July 31, 2025)

Based on mesoscale lattice Boltzmann numerical simulations, we characterize the Rayleigh-Bénard (RB) convective dynamics of dispersions of liquid droplets in another liquid phase. Our numerical methodology allows us to modify the droplets’ interfacial properties to mimic the presence of an emulsifier (e.g., a surfactant), resulting in a positive disjoining pressure that stabilizes the droplets against coalescence. To appreciate the effects of this interfacial stabilization on the RB convective dynamics, we carry out a comparative study between a proper emulsion, i.e., a system where the stabilization mechanism is present (*stabilized* liquid-liquid dispersion), and a system where the stabilization mechanism is absent (*non-stabilized* liquid-liquid dispersion). The study is conducted by systematically changing both the volume fraction, ϕ , and the Rayleigh number, Ra . We find that the morphology of the two systems is dramatically different due to the different interfacial properties. However, the two systems exhibit similar global heat transfer properties, expressed via the Nusselt number Nu . Significant differences in heat transfer emerge at smaller scales, which we analyze via the Nusselt number defined at mesoscales, Nu_{mes} . In particular, stabilized systems exhibit more intense mesoscale heat flux fluctuations due to the persistence of fluid velocity fluctuations down to small scales, which are instead dissipated in the interfacial dynamics of non-stabilized dispersions. For fixed Ra , the difference in mesoscale heat flux fluctuations depends non-trivially on ϕ , featuring a maximum in the range $0.1 < \phi < 0.2$. Taken all together, our results highlight the role of interfacial physics in mesoscale convective heat transfer of complex fluids.

Keywords: Emulsions, multiphase flows, Rayleigh-Bénard thermal convection

I. INTRODUCTION

Emulsions are dispersions of liquid droplets in another liquid phase, stabilized by a surfactant that inhibits droplet coalescence [1–6], thus resulting in a non-trivial collective response of the system when solicited with an external forcing [7, 8]. Emulsions are encountered in a plethora of settings, ranging from food [9] and pharmaceutical industrial processes [10], to geophysics [11] and energy technology [12]. However, their behavior in thermal flows is still poorly understood. The study of thermally driven emulsions – and more generally thermally driven soft materials – finds important applications in geophysics to simulate, for instance, mantle convection from the interior to the planet surface [11, 13–16]; in petrochemical industry [17], where this kind of materials are central to enhanced oil recovery, separation, and refining operations and where temperature-dependent interfacial behavior and rheology affect flow, phase stability, and energy efficiency [18]; in food industry [19], where stability and nutrient maintenance may be altered by heat transfer induced in emulsion-based aliments. Recently, emulsions have found applications as working

fluids in heat exchangers, especially in combination with microencapsulated phase change materials [20, 21].

From the point of view of fundamental fluid mechanics the problem is outstanding: we are dealing with thermal flows and the associated instabilities [22–24], where velocity and thermal fluctuations are non trivially coupled and produce complex time-dependent flows featuring multiscale properties [25–33]; the complexity of the flow is two-way coupled with a dispersion of deformable droplets. Depending on flow conditions, droplets can further undergo break-up and/or coalescence [34–49], thus resulting in dynamical morphological changes in the emulsion. Due to this complexity, theoretical analyses, if any, exist only limited to simple systems [50–57]. Moreover, experiments could face several limitations in exploring thermal convection in emulsions as a result of both the complex nature of these materials and technical limitations. On the one hand, controlling the stability and droplet size distribution over time is challenging, as emulsions are prone to coalescence [58], phase inversion [59, 60], and Ostwald ripening [61], whereas, on the other hand, optical opacity limits flow visualization and measurement [62]. As a result, numerical simulations [56, 63–72] often remain the most effective, and sometimes the only, means to investigate the intricate dynamics of multiphase and

* francesca.pelusi@cnr.it

droplet-laden thermal flows. Indeed, various numerical studies were conducted to characterize the heat transfer properties in different kinds of dispersions, such as thermally bounded convective flows laden with droplets [47, 48, 70, 73] or bubbles (the limiting situation of droplets with negligible internal viscosity) [74–77], thermally-driven multilayer configurations [43, 78], also with different boundary conditions [79]. These studies revealed that dispersed objects (droplets/bubbles) can impact thermal plumes, heat transfer properties, and energy transfer at small scales. Other studies considered the thermal behavior of shear thinning/non-Newtonian [51, 54] or viscoplastic fluids with a finite yield-stress [50, 52, 53, 55, 56, 65, 66, 68, 80], without explicitly considering the presence of dispersed droplets, but rather accounting for their presence via an effective remodulation of the constitutive relation between the shear-rate and the stress in the continuum equations. These studies highlighted the importance of the role that the non-Newtonian rheology – and in particular a finite yield stress [8] – has on the flow initiation and the subsequent thermal plumes dynamics. Still, these studies did not explicitly consider break-up and/or coalescence of droplets and/or their plasticity at mesoscales [81, 82], which have a non-trivial impact in thermally convective flows, as highlighted by experiments on yield-stress fluids [68, 83] and recent numerical simulations by the authors [49, 84]. In particular, the interplay between droplet break-up/coalescence and buoyancy forces gives rise to a variety of thermal convection regimes, depending on the droplet concentration ϕ and intensity of buoyancy [49]: for larger values of ϕ , coalescence phenomena dominate dynamics, eventually leading to phase inverted states exhibiting an intermittent transient dynamics [84]; for sufficiently large buoyancy forces, phase inversion inevitably accompanies a sustained convection; finally, when ϕ is small, break-up phenomena dominates dynamics.

An essential ingredient in the preparation of emulsions is the presence of an emulsifier (i.e., surfactant), which produces a positive disjoining pressure inside the thin liquid film between the interfaces of two adjacent droplets [1, 85, 86]. This disjoining pressure results in an interfacial stabilization mechanism that prevents the coalescence of droplets, leading to the formation of emulsions as stabilized liquid-liquid dispersions [2–6]. This mechanism is crucially influential in the physics of emulsions, especially under concentrated conditions, where droplet-droplet contacts are favored and a closely packed droplet configuration would otherwise be unfeasible. Moreover, the capability of storing elastic energy among neighbouring deformable droplets [87–89], endows the emulsion with non-Newtonian rheological properties [8]. This feature leads to a *distinctive* difference, both morphologically and rheologically, between stabilized and non-stabilized liquid-liquid dispersions. The latter, in particular, cannot sustain high droplet volume fraction and, therefore, are inherently Newtonian. In the setting

of convective thermal flows, it is then natural to expect different dynamical behaviors, a fact that has not been systematically highlighted in the literature so far. Our paper aims to fill this gap. Using hydrodynamic numerical simulations based on the lattice Boltzmann method (LBM) and working in the paradigmatic setup of Rayleigh-Bénard (RB) convection [22–24, 27–29, 90], we simulate the buoyancy-driven dynamics of a stabilized liquid-liquid dispersion (i.e., a proper emulsion), as discussed in previous studies [49, 70, 73, 84], and we compare it with the dynamics of a non-stabilized liquid-liquid dispersion, missing a positive disjoining pressure. We explore the various emerging dynamical regimes by changing the volume fraction of dispersed phase, ϕ , and the buoyancy force, quantified in terms of the dimensionless Rayleigh number, Ra . We analyze both the heat flux and the system morphology (via the use of interface indicators) at changing ϕ and Ra . We find that the morphologies of the two systems significantly differ; however, the dependence of the *global* heat flux properties on ϕ and Ra does not seem sensitive to the physicochemical characteristics of the dispersion (namely, whether it is stabilized or not). A *mesoscale* analysis of the heat flux properties reveals, instead, a mismatch between the two systems, featuring enhanced fluctuations in the stabilized system for all volume fractions $\phi < 0.5$, with a maximum relative increase at a (Ra -dependent) volume fraction in the range $0.1 < \phi < 0.2$. The presence of a maximum is arguably related to the coupling between small-scale velocity fluctuations and interface dynamics, which is markedly impacted by the interfacial stabilization.

The paper is organized as follows: in Sec. II, we describe the system setup, introduce the dimensionless control parameters, and provide a summary of the LBM employed. Results of numerical simulations are shown in Sec. III. Finally, conclusions are given in Sec. IV.

II. MODEL AND SIMULATIONS

We first describe the hydrodynamic setup and associated dimensionless numbers considered in the numerical simulations in Sec. II A; we then review the numerical methodology used in Sec. II B.

A. Hydrodynamical setup and dimensionless parameters

For both stabilized and non-stabilized liquid-liquid dispersions, we consider a collection of dispersed (d) liquid droplets with kinematic viscosity ν in another equiviscous carrier (c) liquid in a two-dimensional setup of RB thermal convection [27, 29, 90] with coordinates (x, z) , wherein two parallel plates of length L extending in the x direction are placed at distance H and located

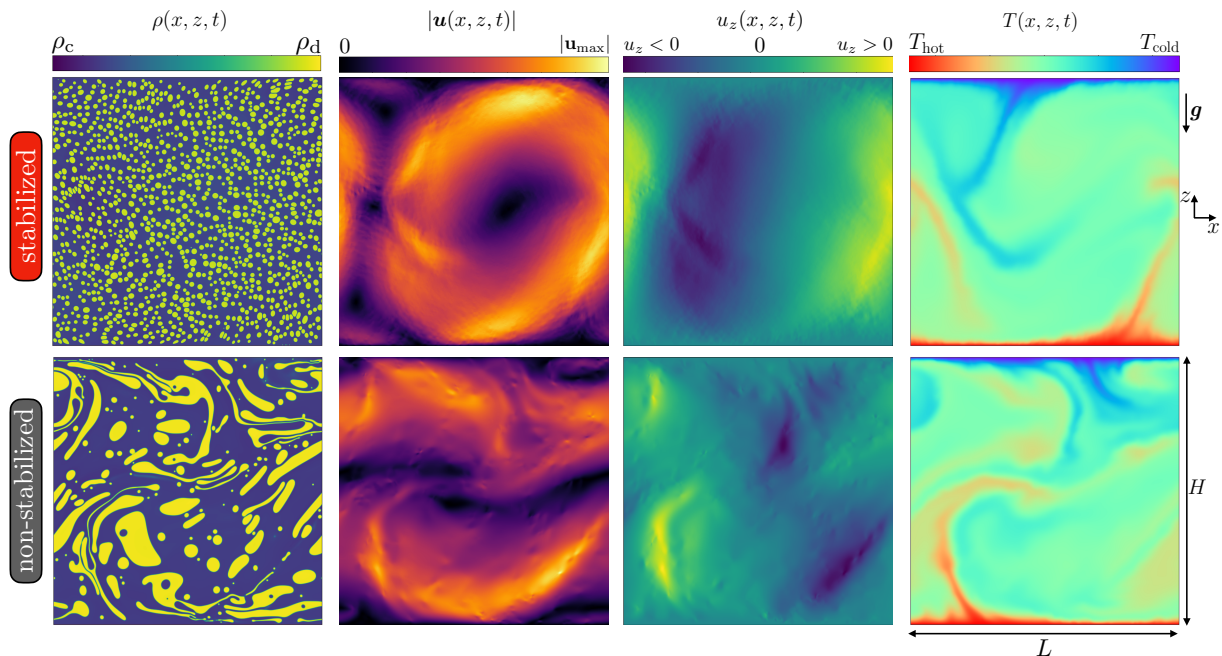


FIG. 1. Representative snapshots of the dynamics of the Rayleigh-Bénard (RB) thermal convection of stabilized and non-stabilized liquid-liquid dispersions. Systems are confined between a lower hot and an upper cold wall at a distance H , thus undergoing a temperature difference $\Delta T = T_{\text{hot}} - T_{\text{cold}}$. A buoyancy force is applied due to the gravity \mathbf{g} . Convective states are analyzed by investigating the hydrodynamical fields of density $\rho(x, z, t)$, velocity $\mathbf{u}(x, z, t)$, and temperature $T(x, z, t)$. Snapshots refer to systems with a volume fraction $\phi = 0.28$ and Rayleigh number $\text{Ra} \approx 1.6 \times 10^7$.

at $z = \pm H/2$ (see Fig. 1). In contrast to previous works [49, 70, 73, 84], where simulations were performed with an aspect ratio $\Gamma = L/H = 2$, we adopted a fixed aspect ratio of $\Gamma = 1$ throughout this study (that is, $H = L$). This choice is motivated by limitations observed in the non-stabilized liquid-liquid dispersion at low values of Ra , where, for larger Γ (i.e., larger confinement), the dispersed phase tends to remain trapped within the two dominant convective rolls. By setting $\Gamma = 1$, we mitigate this confinement effect, whose details are worth being studied in a separate work. The system is heated from below and cooled from above, fixing at all times (t) the bottom and upper plate temperatures at $T(x, z = -H/2, t) = T_{\text{hot}}$ and $T(x, z = +H/2, t) = T_{\text{cold}}$, resulting in a temperature jump $\Delta T = T_{\text{hot}} - T_{\text{cold}}$; periodic boundary conditions are applied in the x direction (see Fig. 1).

The dispersed and carrier phases are described by density fields $\rho_{d,c}(x, z, t)$; as detailed below, the methodology used for the numerical simulations implies diffuse interfaces, i.e., an interface with small (but finite) thickness that separates regions with the majority of the dispersed phase ($\rho_d \gg \rho_c$) from regions with the majority of the carrier phase ($\rho_d \ll \rho_c$). Further, the presence of interfaces is associated with a surface tension Σ . The initial configuration consists of N_d droplets with a predefined spatial arrangement, which is generated through a preparatory simulation [49, 91]: the centers-of-mass of the droplets are initially positioned in a honeycomb-like

pattern, and we assign to the droplets a circular geometry of diameter d . Then, to introduce disorder and facilitate a physically realistic setup, small random perturbations are applied to both the droplets' initial centers-of-mass positions and the density field of the surrounding continuous liquid. The system is then allowed to evolve freely with no applied forcing, relaxing towards a lower-energy configuration, thus reaching a slightly poly-disperse droplet size distribution. The resulting system is then identified with the volume fraction

$$\phi = \frac{A_d}{LH}, \quad (1)$$

where A_d is the total area occupied by the dispersed phase. In the presence of diffuse interfaces, we need to introduce a threshold to compute A_d as $A_d = \int \int \Theta(\rho_d(x, z) - \rho^*) dx dz$, where Θ is the Heaviside step function and ρ^* is a threshold value corresponding to the mean value between the dispersed and carrier phase in the bulk region [70, 73]. We distinguish between stabilized and non-stabilized liquid-liquid dispersions by introducing a mechanism that promotes, in the former case, the emergence of a positive disjoining pressure in the thin liquid films separating closely adjacent interfaces, which inhibits droplet coalescence. Then, gravity acts in the negative z direction with strength g , resulting in a buoyancy force density equal to $\rho\alpha(T - T_0)g$, where T_0 is a reference temperature [92], $\rho = \rho_d + \rho_c$ is the total density, and α is the thermal expansion coefficient. Once the droplets are placed in the desired initial condition

with a given volume fraction ϕ , we apply a suitable sinusoidal perturbation to the velocity field to trigger convection [84]. Convective states are analyzed via the hydrodynamical velocity, $\mathbf{u}(x, z, t)$, the density of the dispersed and carrier phase, $\rho_{d,c}(x, z, t)$, and the temperature field $T(x, z, t)$ (see Fig. 1). The dynamics of the temperature field $T(x, z, t)$ is governed by an advection-diffusion equation, with the advection set by the hydrodynamical velocity and the diffusion regulated by a constant thermal diffusivity κ . In all numerical simulations, we use, as input parameters, the volume fraction ϕ defined in Eq. (1) and the Rayleigh number, [24, 27–29, 93]

$$\text{Ra} = \frac{\alpha g \Delta T H^3}{\nu \kappa}, \quad (2)$$

which encodes the buoyancy intensity. The Prandtl number ν/κ is kept fixed in all simulations. Notice that, in contrast to homogeneous fluids, stabilized liquid-liquid dispersions exhibit a response to external forcing that is significantly influenced by interfacial effects, the latter altering the viscous, elastic, and visco-plastic properties of the system. Consequently, Ra in Eq. (2) loses its dynamical meaning for the stabilized case as the volume fraction ϕ increases, since the effective viscosity of the system becomes sensitive to the local shear rate. Therefore, throughout this work, we define both Ra and Pr considering the kinematic viscosity of the corresponding homogeneous reference fluid with $\rho_d = \rho_c$. Under this convention, Ra remains a dimensionless parameter that quantifies the intensity of the applied buoyancy. We assume no variation in surface tension Σ between the two systems under comparison (see Sect. II B for details). As a consequence, we do not consider the Weber number, $\text{We} = \rho U^2 d / \Sigma$ (U is the characteristic flow velocity), as an independent control parameter, because Ra directly determines it in this context [94].

To monitor the heat transfer properties, in every point $\mathbf{x} = (x, z)$ and for any time t we compute the corresponding local Nusselt number as

$$\text{Nu}(\mathbf{x}, t) = 1 + \frac{u_z(\mathbf{x}, t) T(\mathbf{x}, t)}{\kappa \frac{\Delta T}{H}}, \quad (3)$$

and we average in space to obtain the global Nusselt number Nu [27, 29, 95, 96]

$$\text{Nu}(t) = \langle \text{Nu}(\mathbf{x}, t) \rangle_{x,z}, \quad (4)$$

where $\langle \dots \rangle_{x,z}$ refers to the spatial average on the overall domain $L \times H$. In the statistically steady state (hereafter referred to as “steady-state”, for brevity), we average the signal $\text{Nu}(t)$ over time, thus computing $\bar{\text{Nu}} = \langle \text{Nu} \rangle_t$. The system morphology is assessed in terms of the interface indicator defined as:

$$\text{I}(t) = \langle |\nabla \chi(\mathbf{x}, t)| \rangle_{x,z}, \quad \chi(\mathbf{x}, t) = \frac{\rho_d(\mathbf{x}, t) - \rho_c(\mathbf{x}, t)}{\rho_d(\mathbf{x}, t) + \rho_c(\mathbf{x}, t)}, \quad (5)$$

where χ is the phase field. Similarly to the study of heat transfer, we average $\text{I}(t)$ over time when focusing on steady-state properties, obtaining $\bar{\text{I}} = \langle \text{I} \rangle_t$.

B. Lattice Boltzmann model

Simulations are carried out using the lattice Boltzmann methods (LBMs) [97–99], which are computational tools capable of accurately capturing the behavior of multiphase and multicomponent systems [45, 70–72, 84, 100–106]. Particularly, we employ the open-source code **TLBfind** [91], featuring the dynamics of a multicomponent system in thermal flows. The essential aspects are summarized below, while a more comprehensive treatment is presented in Ref. [91]. Hereafter, all dimensional quantities are given in lattice Boltzmann simulation units.

The system dynamics is simulated by evolving on a two-dimensional lattice the distribution function $f_{\xi,i}(\mathbf{x}, t)$, which represents the probability of finding a fluid particle of phase $\xi = d, c$ with discrete velocity \mathbf{c}_i [107] at location $\mathbf{x} = (x, z)$ and time t . Spatial and temporal spacings are set to $\Delta x = \Delta t = 1$, respectively. The dynamical evolution of $f_{\xi,i}$ is governed by the lattice Boltzmann equation

$$f_{\xi,i}(\mathbf{x} + \mathbf{c}_i, t+1) - f_{\xi,i}(\mathbf{x}, t) = -\frac{1}{\tau} \left[f_{\xi,i}(\mathbf{x}, t) - f_{\xi,i}^{(\text{eq})}(\mathbf{x}, t) \right], \quad (6)$$

where $f_{\xi,i}^{(\text{eq})}$ is a local equilibrium distribution function, $f_{\xi,i}^{(\text{eq})}(\mathbf{x}, t) = f_{\xi,i}^{(\text{eq})}(\rho_\xi(\mathbf{x}, t), \bar{\mathbf{u}}_\xi(\mathbf{x}, t))$, whose dependence from the density ρ_ξ and velocity $\bar{\mathbf{u}}_\xi$ is set by

$$f_{\xi,i}^{(\text{eq})}(\rho_\xi, \bar{\mathbf{u}}_\xi) = w_i \rho_\xi \left[1 + \frac{\bar{\mathbf{u}}_\xi \cdot \mathbf{c}_i}{c_s^2} - \frac{\bar{\mathbf{u}}_\xi \cdot \bar{\mathbf{u}}_\xi}{2c_s^2} + \frac{(\bar{\mathbf{u}}_\xi \cdot \mathbf{c}_i)^2}{2c_s^4} \right]. \quad (7)$$

The distribution function $f_{\xi,i}$ relaxes towards the local equilibrium $f_{\xi,i}^{(\text{eq})}$ with a relaxation time τ [108]. In Eq. (7), $c_s = 1/\sqrt{3}$ is the lattice speed of sound and w_i are model-dependent weights [91, 98, 99] [109]. The macroscopic density and velocity fields can be computed directly from $f_{\xi,i}$ as

$$\rho_\xi(\mathbf{x}, t) = \sum_{i=0}^8 f_{\xi,i}(\mathbf{x}, t), \quad (8)$$

$$\mathbf{u}(\mathbf{x}, t) = \frac{1}{\rho(\mathbf{x}, t)} \sum_{\xi} \sum_{i=0}^8 \mathbf{c}_i f_{\xi,i}(\mathbf{x}, t),$$

with $\rho = \sum_{\xi} \rho_\xi$ being the total density. Initial densities of the carrier and dispersed liquids are set to $\rho_{d,c}^{\text{max}} = 1.18$ and $\rho_{d,c}^{\text{min}} = 0.18$, respectively. Working in the framework of Shan-Chen pseudopotential LBMs [110–113], external and internal forces \mathbf{F}_ξ acting on each component are incorporated in the dynamics (Eq. (6)) via the equilibrium velocity $\bar{\mathbf{u}}_\xi$ entering in Eq. (7), as

$$\bar{\mathbf{u}}_\xi(\mathbf{x}, t) = \mathbf{u}(\mathbf{x}, t) + \frac{\tau \mathbf{F}_\xi(\mathbf{x}, t)}{\rho_\xi(\mathbf{x}, t)}. \quad (9)$$

Notice that the LBM framework reproduces the Navier-Stokes equations for the hydrodynamic velocity $\mathbf{u} = \mathbf{u} +$

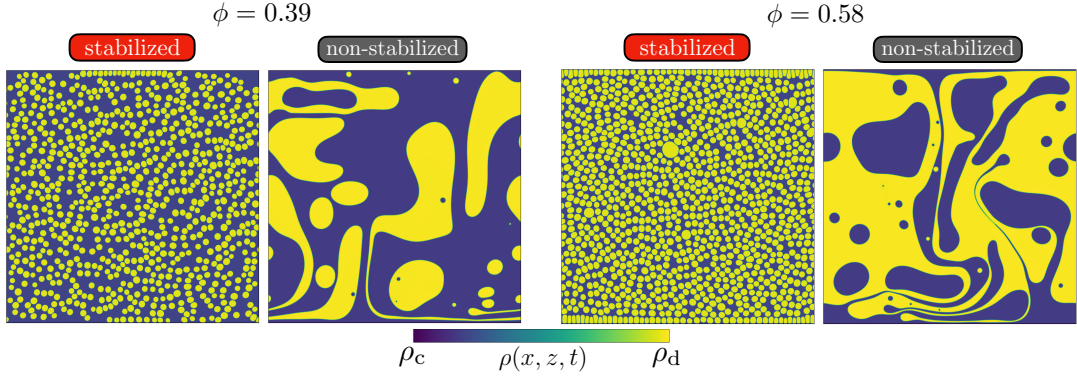


FIG. 2. Comparison between stabilized and non-stabilized liquid-liquid dispersions at varying volume fractions ϕ . The selected values of ϕ are chosen in such a way that $|\phi - \bar{\phi}| \approx 0.1$, with $\bar{\phi} = 0.5$. While non-stabilized systems exhibit morphological symmetry under the exchange of continuous and dispersed phases, stabilized liquid-liquid dispersions break this symmetry due to the presence of a disjoining pressure. All snapshots correspond to simulations at $Ra \approx 1.6 \times 10^6$.

$\mathbf{F}/2\rho$, with a kinematic viscosity $\nu = c_s^2(\tau - 1/2)$ [98, 99]. In Eq. (9), \mathbf{F}_ξ encompasses several contributions to the interaction as

$$\mathbf{F}_\xi(\mathbf{x}, t) = \mathbf{F}_\xi^{\text{intra}}(\mathbf{x}, t) + \mathbf{F}_\xi^{\text{inter}}(\mathbf{x}, t) + \mathbf{F}_\xi^{\text{ext}}(\mathbf{x}, t). \quad (10)$$

Specifically, $\mathbf{F}_\xi^{\text{intra}}$ encodes the intra-component interactions and its definition is based on the pseudo-potential ψ :

$$\mathbf{F}_\xi^{\text{intra}}(\mathbf{x}, t) = -G_{\text{dc}}\psi_\xi(\mathbf{x}, t) \sum_{i=0}^8 w_i \psi_{\xi'}(\mathbf{x} + \mathbf{c}_i, t) \mathbf{c}_i, \quad (11)$$

where $\xi' \neq \xi$, $\psi_{\xi, \xi'} = \rho_{\xi, \xi'}/\rho_0$ (ρ_0 is a reference density value [114]). This interaction leads to phase separation and the formation of interfaces, thus the coupling parameter G_{dc} primarily controls the surface tension Σ at the interface. Furthermore, $\mathbf{F}_\xi^{\text{inter}}$ includes both short-range attractive and mid-range repulsive forces within the same component

$$\begin{aligned} \mathbf{F}_\xi^{\text{inter}}(\mathbf{x}, t) = & -G_{\xi\xi}^a \psi_\xi(\mathbf{x}, t) \sum_{i=0}^8 w_i \psi_\xi(\mathbf{x} + \mathbf{c}_i, t) \mathbf{c}_i \\ & - G_{\xi\xi}^r \psi_\xi(\mathbf{x}, t) \sum_{i=0}^{24} p_i \psi_\xi(\mathbf{x} + \mathbf{c}_i, t) \mathbf{c}_i, \end{aligned} \quad (12)$$

where $G_{\xi\xi}^a < 0$, $G_{\xi\xi}^r > 0$ are interaction parameters, p_i are weights over an extended lattice set [91, 112], and the pseudo-potential ψ_ξ follows the original Shan-Chen form $\psi_\xi = \rho_0(1 - \exp(-\rho_\xi/\rho_0))$ [110]. Eq. (12) constitutes the key feature of the model adopted in this work, as it effectively mimics the stabilizing role of surfactants at fluid interfaces by producing a positive disjoining pressure in the thin liquid films separating close-by interfaces [101, 113]. As discussed earlier, this tends to prevent droplet coalescence, thereby enabling the formation of stabilized liquid-liquid dispersions. Stabilized liquid-liquid dispersions are obtained by setting the interaction

parameters to $G_{\text{cc}}^a = -9.0$, $G_{\text{dd}}^a = -8.0$, $G_{\text{cc}}^r = 8.1$, and $G_{\text{dd}}^r = 7.1$, whereas they are set equal to zero in the non-stabilized case. It is also important to note that turning off the inter-component interactions (cfr. Eq. (12)) alters the effective surface tension Σ . Hence, to ensure consistency between the two scenarios, i.e., to recover the exact value of $\Sigma \sim 0.0325$, we set $G_{\text{dc}} = 0.405$ for the stabilized liquid-liquid dispersion. In contrast, the value was increased to $G_{\text{dc}} = 0.65$ in the non-stabilized case. In other words, force contributions in Eq. (12) allow to switch from a stabilized liquid-liquid dispersion to a non-stabilized one in the same computational framework.

The dynamics of the temperature field $T = T(\mathbf{x}, t)$ is incorporated into the model by adding a distribution function, $h_i(\mathbf{x}, t)$, which is governed by a dedicated lattice Boltzmann equation [98, 99]:

$$h_i(\mathbf{x} + \mathbf{c}_i, t+1) - h_i(\mathbf{x}, t) = -\frac{1}{\tau_h} [h_i(\mathbf{x}, t) - h_i^{(\text{eq})}(\mathbf{x}, t)], \quad (13)$$

where τ_h is the associated relaxation time and $h_i^{(\text{eq})}$ is the local equilibrium distribution function, $h_i^{(\text{eq})}(\mathbf{x}, t) = h_i^{(\text{eq})}(T(\mathbf{x}, t), \mathbf{u}(\mathbf{x}, t))$, whose dependency from the temperature T and velocity \mathbf{u} is set by:

$$h_i^{(\text{eq})}(T, \mathbf{u}) = w_i T \left[1 + \frac{\mathbf{u} \cdot \mathbf{c}_i}{c_s^2} - \frac{\mathbf{u} \cdot \mathbf{u}}{2c_s^2} + \frac{(\mathbf{u} \cdot \mathbf{c}_i)^2}{2c_s^4} \right]. \quad (14)$$

Similarly to the fluid case, the macroscopic temperature $T(\mathbf{x}, t)$ is obtained as the zeroth-order moment of the distribution h_i , i.e.,

$$T(\mathbf{x}, t) = \sum_{i=0}^8 h_i(\mathbf{x}, t). \quad (15)$$

Thermal effects enter the dynamics of both fluid components through a buoyancy forcing term modeled via an external force $\mathbf{F}_\xi^{\text{ext}}$ in Eq. (10) expressed in the Boussinesq approximation [115]:

$$\mathbf{F}_\xi^{\text{ext}}(\mathbf{x}, t) = -\rho_\xi(\mathbf{x}, t) \alpha g T(\mathbf{x}, t). \quad (16)$$

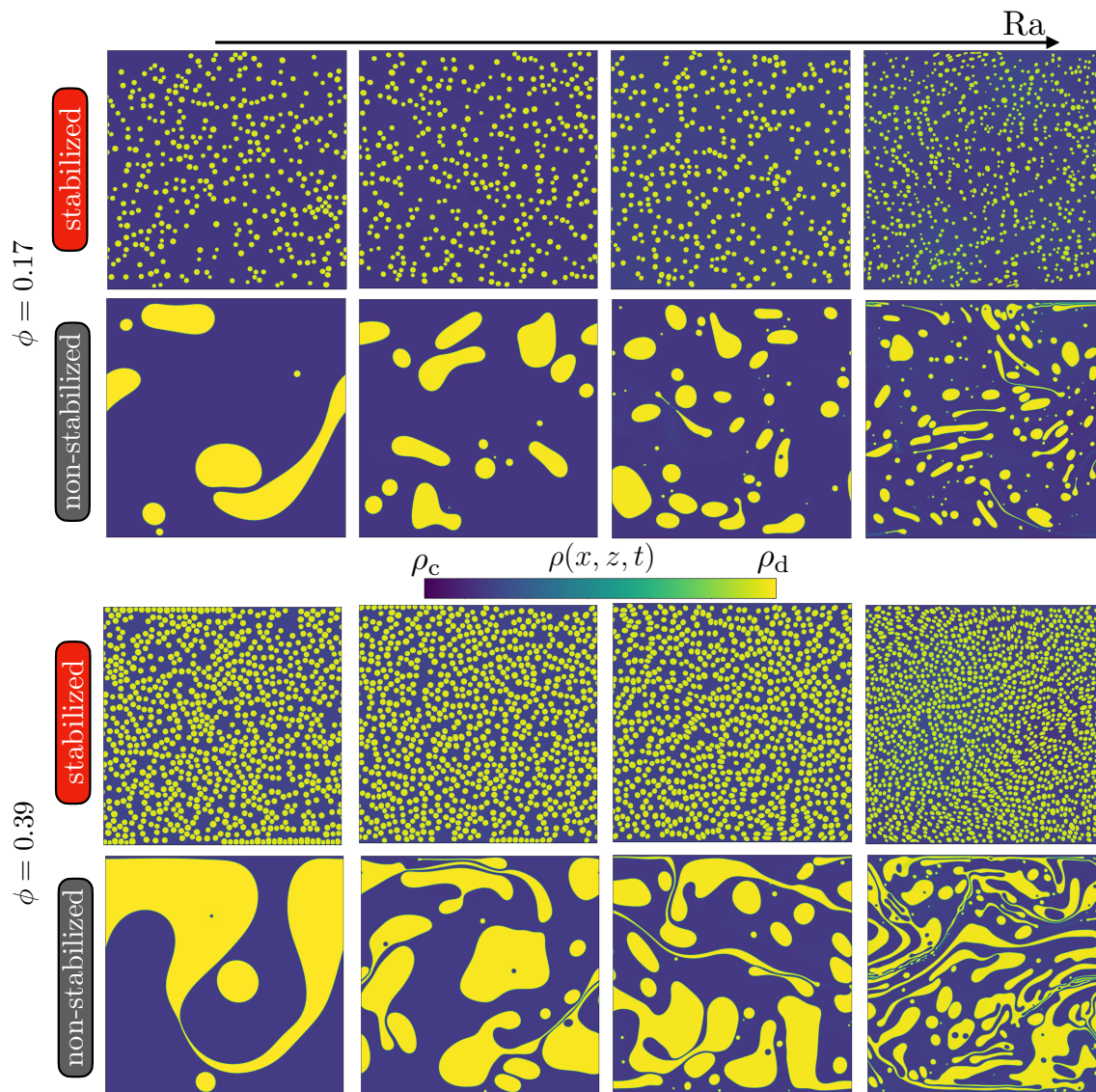


FIG. 3. Density map snapshots for different volume fractions ϕ and different Rayleigh numbers Ra , featuring both stabilized and non-stabilized liquid-liquid dispersions. Ra increases from left to right.

On the hydrodynamic scale, this formulation allows us to solve an advection-diffusion equation for T , where the temperature is advected by the fluid velocity \mathbf{u} and the thermal diffusivity is given by $\kappa = c_s^2(\tau_h - 1/2)$.

Simulations are conducted on a 2048×2048 lattice grid. Droplets are initialized with a diameter $d \sim 50$ lattice spacings. Regarding boundary conditions, bounce-back rules are applied along the z direction to both fluid components to enforce no-slip conditions at walls. At the same time, the temperature field is subject to Dirichlet conditions at the top and bottom boundaries [98, 99].

We performed numerical simulations employing Nvidia A30 GPUs. In total, we carried out approximately 120 distinct numerical simulations, each typically requiring ~ 48 GPU-hours. The simulation time, expressed in units of the characteristic free-fall time $t_{FF} \sim \sqrt{H/\alpha g \Delta T}$,

varies according to the strength of the imposed buoyancy force: t_{FF} spans from roughly 6.4×10^3 (for $Ra \approx 1.6 \times 10^7$) up to about 4.5×10^4 (for $Ra \approx 3.5 \times 10^5$). Once the steady-state is attained, time-averaged quantities are computed over intervals ranging from 14 to $800 t_{FF}$, depending on Ra . For the analysis of mesoscale observables, we gather statistics by including all droplets observed throughout the steady-state regime at all recorded time steps.

III. RESULTS AND DISCUSSION

We restrict our analysis to volume fractions $\phi < 0.5$, due to the impossibility to pack droplets beyond this value of concentration in the non-stabilized case; for $\phi > 0.5$ the

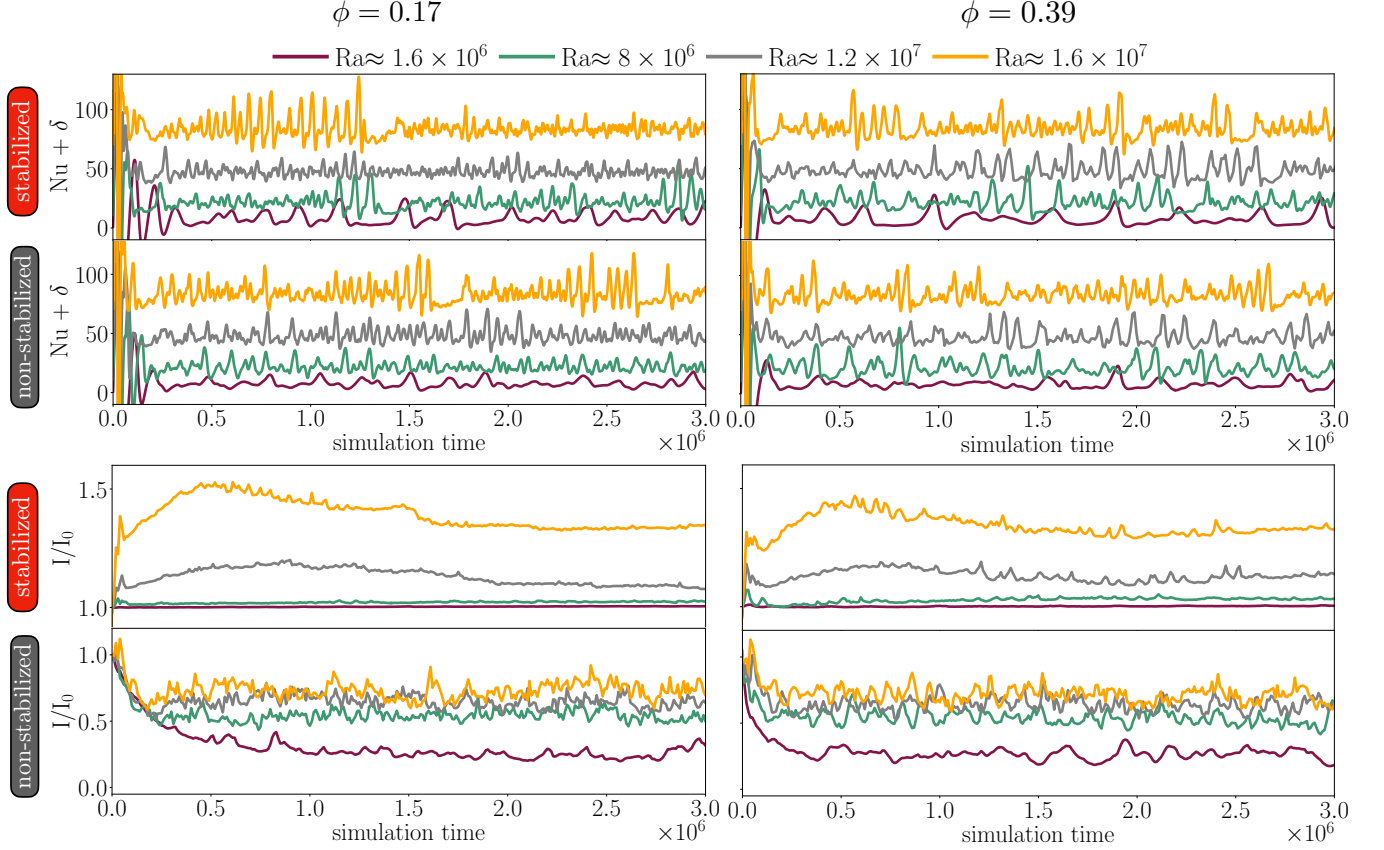


FIG. 4. Time evolution of the Nusselt number Nu (cfr. Eq. (4)) and the interface indicator I (cfr. Eq. (5)), normalized with its initial value I_0 , for stabilized and non-stabilized liquid-liquid dispersions. Left panels refer to cases with a volume fraction $\phi = 0.17$. Right panels refer to the case with $\phi = 0.39$. Different values of the Rayleigh number Ra (different colors) are considered. To facilitate readability, data for Nu are vertically shifted by a quantity δ which depends on Ra : $\delta = 0$ for $Ra \approx 1.6 \times 10^6$, $\delta = 10$ for $Ra \approx 8 \times 10^6$, $\delta = 35$ for $Ra \approx 1.2 \times 10^7$, while $\delta = 70$ for $Ra \approx 1.6 \times 10^7$.

dispersion would unavoidably undergo a phase inversion with droplet (of initially continuous phase) concentration $1 - \phi$, for any forcing (see Fig. 2). In other words, non-stabilized dispersions can only exist with the minority phase being dispersed and under a non-zero forcing (otherwise full phase separation would occur [116]). Stabilized dispersions, instead, can be prepared across the whole concentration range $0 < \phi < 1$, being stable against phase separation and prone to phase inversion only if the forcing is large enough to overcome the barrier imposed by the disjoining pressure [49, 70, 73]. We collect data at varying the control parameters ϕ and Ra . Fig. 3 shows a comparison of density map snapshots, in the steady-state, for different combinations of the (ϕ, Ra) pair. As expected, this figure confirms that the presence or absence of an interfacial stabilization mechanism crucially affects the morphology of the dispersions: the stabilized dispersion mostly consists of many, essentially round, small droplets, whereas the non-stabilized dispersion develops domains that are, on average, bigger and more anisotropic. This qualitative comparison raises important questions about how the nature of dispersion in-

fluences both heat transfer performance and morphological organization. To answer them, we investigate the time evolution of the heat transfer, encoded in the Nusselt number Nu (cfr. Eq. (4)), and the amount of interface, encoded in the interface indicator I (cfr. Eq. (5)). Results are reported in Fig. 4 for different combinations of the pair (ϕ, Ra) . For fixed Ra and nature of dispersion, the time evolutions of Nu for different ϕ (top panels) look similar, despite heat flux fluctuations appearing more pronounced in the more diluted case. This scenario is representative of a Newtonian homogeneous fluid while approaching turbulence [49, 117]. However, when comparing stabilized and non-stabilized systems at fixed pair (ϕ, Ra) , we observe similar time evolutions of Nu , a behavior which is also reflected in kinetic energy signals (data not shown). Despite the time evolutions of Nu look qualitatively similar (see also Fig. 5), the scenario changes when we analyze the dispersion morphology via the interface indicator I at fixed pair (ϕ, Ra) . Indeed, the time evolutions of I (bottom panels) highlight the distinct physical mechanisms that lead to the steady-state configuration. On the one hand, the stabilized liquid-liquid

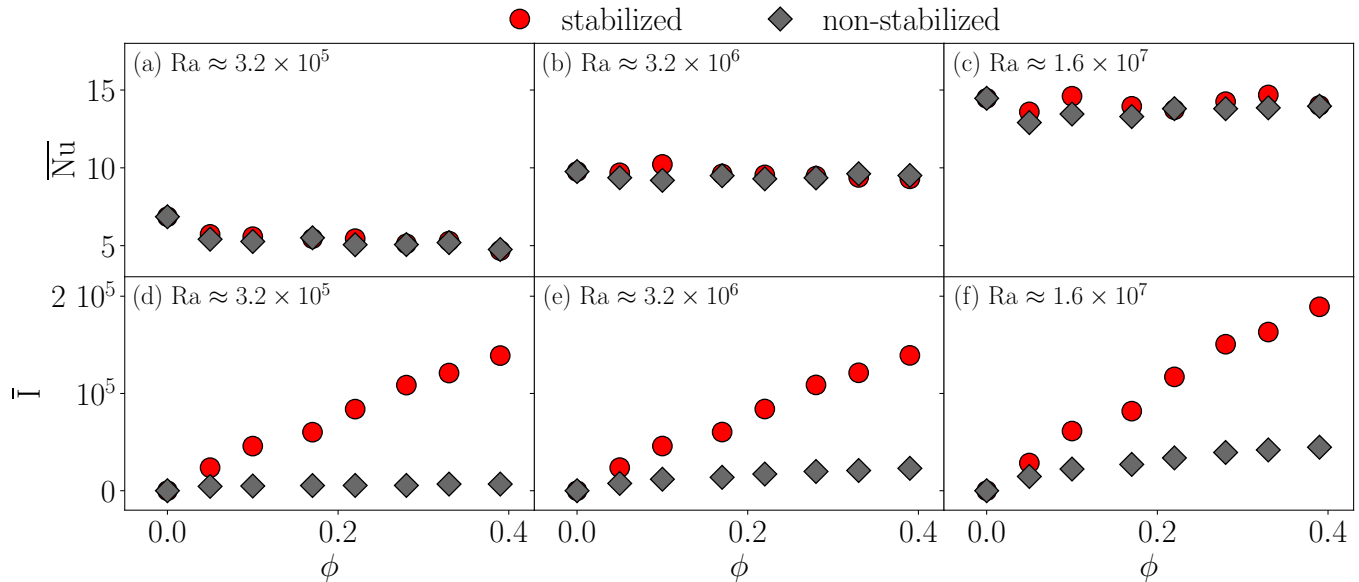


FIG. 5. Steady-state averages in time of the Nusselt number \overline{Nu} (panels (a)-(c)), and the interface indicator \bar{I} (panels (d)-(f)) as a function of the volume fraction ϕ , for different values of the Rayleigh number Ra . Data for both stabilized (red circles) and non-stabilized (grey diamonds) liquid-liquid dispersions are shown.

dispersion does not sensibly vary its morphology unless the buoyancy amplitude is large enough and the system enters a breakup-dominated regime [49]. On the other hand, the non-stabilized liquid-liquid dispersion is inherently prone to coalescence at any value of Ra , leading to a progressive reduction of the total interfacial area over time, until the steady-state is reached. To summarize, in the dilute regime, a variation in ϕ or the nature of dispersion does not appear to impact the global heat transfer properties of the system; however, the amount of interface evolves according to different physical mechanisms, leading to distinct steady-state configurations.

We next investigate the time average over the steady state of the relevant observables, for various combinations of the (ϕ, Ra) pair. In Fig. 5, we report \overline{Nu} and \bar{I} as a function of ϕ , for different values of Ra . First, we notice that, in the range of Ra explored, \overline{Nu} (which grows with Ra , as expected) is essentially independent of the volume fraction and the nature of dispersion [Fig. 5(a)-(c)]. A naive interpretation of this behavior might suggest that, for low to moderate volume fractions ($\phi < 0.5$), where non-Newtonian effects are absent or negligible, an increase of ϕ leads to a higher effective viscosity of the system and, consequently, to a monotonic decrease in the average heat flux. However, this simplistic view neglects the crucial role played by the presence of finite-size droplets in modulating heat transfer. Considering emulsions in the range $\phi < 0.5$, as previously observed in Ref. [70], the presence of finite-sized droplets introduces mesoscopic interfacial structures that actively interfere with the formation of large-scale thermal plumes and inhibit the convective transport. This inhibition becomes more pronounced at low values of Ra , i.e., just above the

transition from conduction to convection, where the reduction in \overline{Nu} with increasing ϕ (within 10%) is evident but not as steep as one would expect based on viscosity arguments only [70]. However, as Ra increases (see Fig. 5), this reduction in heat transfer is progressively mitigated, indicating a nontrivial interplay between ϕ and Ra . In contrast, recent results by Bilondi et al. [47] focused on non-stabilized liquid-liquid dispersions at sufficiently high values of Ra , and report an enhancement of \overline{Nu} with increasing ϕ , attributed to the amplification of small-scale mixing induced by interfacial stresses. Putting everything together, one would then expect the existence of a non-monotonic transition in the heat transfer behavior when the system is diluted ($\phi < 0.5$), which is governed by both droplet concentration and buoyancy forcing: when Ra is low, \overline{Nu} decreases upon increasing ϕ ; then, for intermediate values of Ra , the heat transfer experiences almost no variation as a function of ϕ ; finally, if the buoyancy is large enough, then it starts to increase. In this context, the heat transfer budget approach introduced in Ref. [47] — which decomposes convective and diffusive contributions from both phases — provides a valuable conceptual tool for interpreting the competing mechanisms governing this transition. In agreement with this view, our results suggest that droplet-scale interfacial dynamics contribute to a reorganization of the energy transport process, subtly modifying how heat is distributed between boundary layers and bulk flow as both ϕ and Ra vary. Although the interfacial stabilization does not have a significant impact on the mean heat transfer, it affects the system morphology. In Fig. 5(d)-(f), this effect is quantified via the analysis of \bar{I} as a function of ϕ for different values of Ra . In

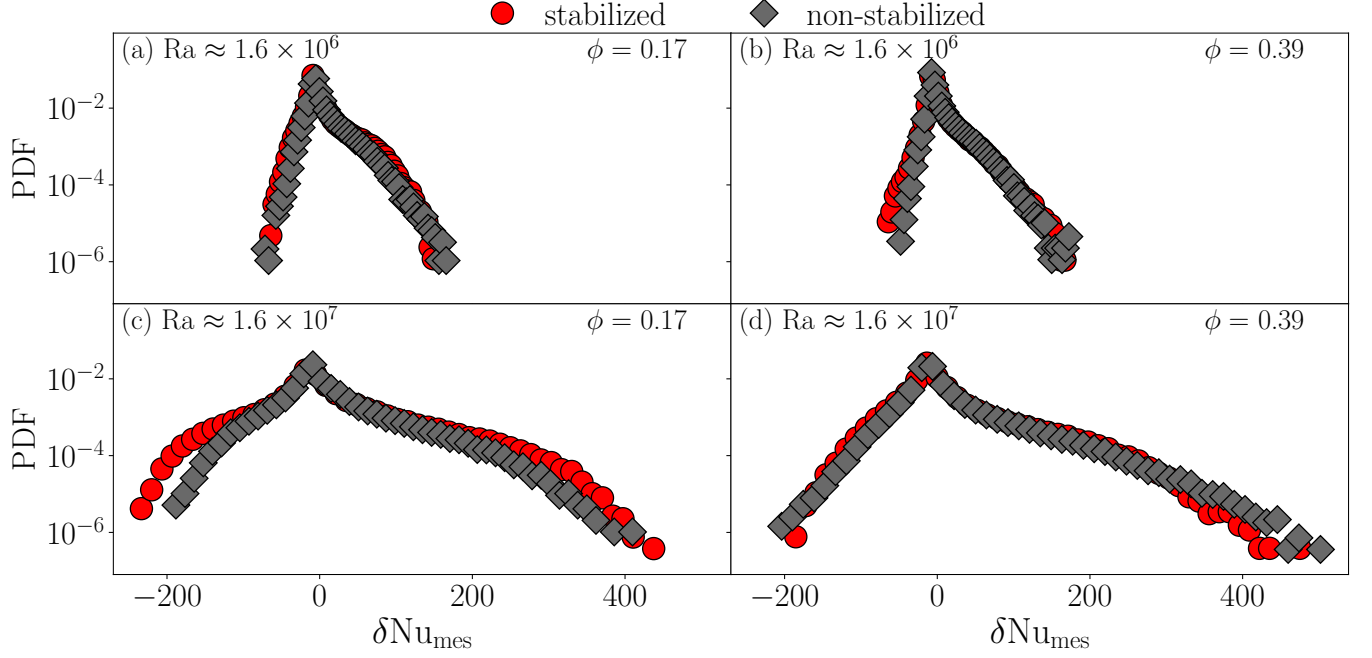


FIG. 6. Probability distribution functions (PDFs) of the fluctuations $\delta \text{Nu}_{\text{mes}}$ of the Nusselt number at mesoscales Nu_{mes} (cfr. Eq. (17)) for different values of the volume fraction (different columns) and different values of the Rayleigh number Ra (different rows). Data for both stabilized (red circles) and non-stabilized (grey diamonds) liquid-liquid dispersions are shown.

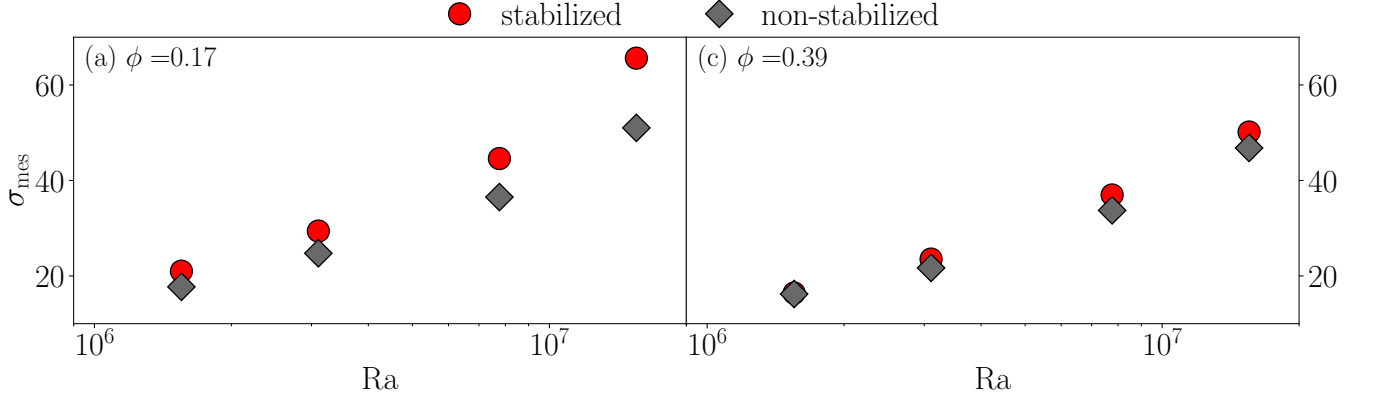


FIG. 7. Standard deviation σ_{mes} of the Nusselt number at mesoscales Nu_{mes} (see text for details) as a function of the Rayleigh number Ra for different values of the volume fraction ϕ . Data for both stabilized (red circles) and non-stabilized (grey diamonds) liquid-liquid dispersions are shown.

the case of the stabilized liquid-liquid dispersion, $\bar{\Gamma}$ exhibits a clear increasing trend with ϕ across all values of Ra . By contrast, in the non-stabilized case, this dependence is much weaker and becomes noticeable only at the highest Ra . This difference directly stems from the inhibition of coalescence in the stabilized dispersion, which preserves a more structured and interface-rich morphology. It is therefore reasonable to expect that such pronounced morphological differences may leave a trace in the heat transfer dynamics, not necessarily in global observables, but rather through small-scale signatures associated with interfacial processes. Bearing these obser-

vations in mind, we move beyond macroscopic observables and examine heat transfer at the mesoscale, i.e., at the characteristic scale of the droplet size. Unlike previous studies on emulsions [70, 73, 84], where droplet-based observables could be defined thanks to the fact that droplets could be identified and followed for a reasonable amount of time during their evolution with a lagrangian tool of analysis [91], here a different approach is needed, since in non-stabilized liquid-liquid dispersions approaching droplets inevitably coalesce, and hence they can't be followed for long times. Thus, we focus on spatial fluctuations of the Nusselt number at mesoscales, de-

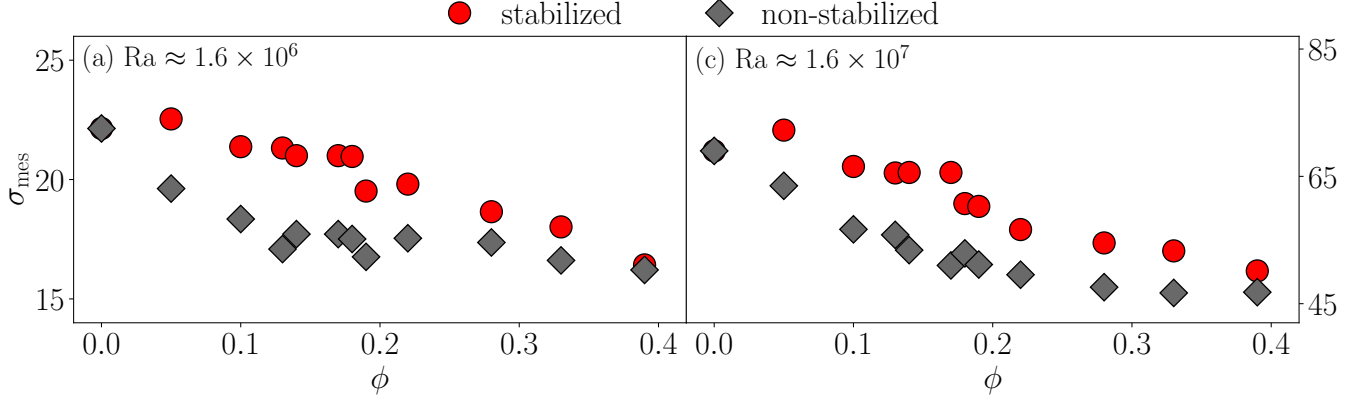


FIG. 8. Standard deviation σ_{mes} of the Nusselt number at mesoscales Nu_{mes} (cfr. Eq. (17)) as a function of the volume fraction ϕ for different values of the Rayleigh number Ra . Data for both stabilized (red circles) and non-stabilized (grey diamonds) liquid-liquid dispersions are shown.

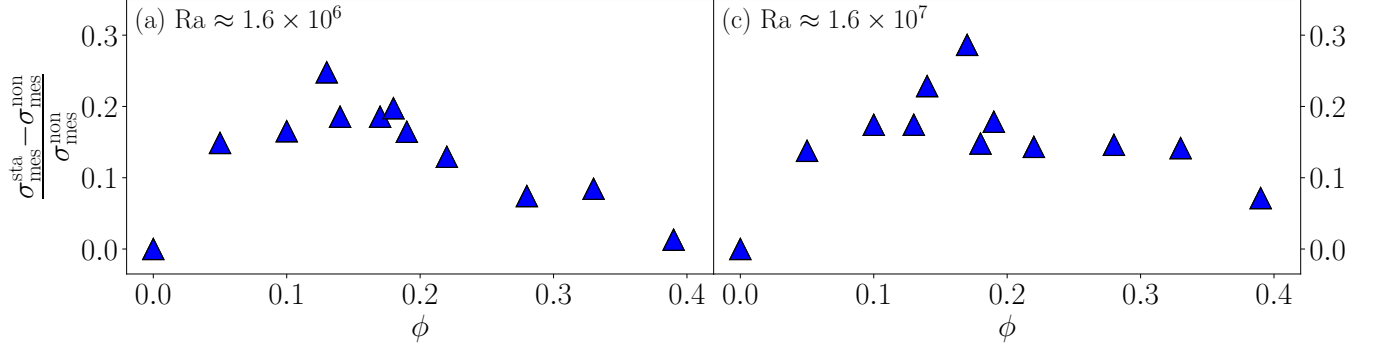


FIG. 9. Normalized difference between standard deviation of the Nusselt number at mesoscales Nu_{mes} (cfr. Eq. (17)) for non-stabilized ($\sigma_{\text{mes}}^{\text{non}}$) and stabilized ($\sigma_{\text{mes}}^{\text{sta}}$) liquid-liquid dispersions as a function of the volume fraction ϕ and for different values of the Rayleigh number Ra .

defined as $\delta Nu_{\text{mes}} = Nu_{\text{mes}} - \langle Nu_{\text{mes}} \rangle$, where $\langle \cdot \rangle$ denotes a combined spatial and temporal average. The mesoscale observable Nu_{mes} is defined as

$$Nu_{\text{mes}}(\mathbf{X}_k) = \int \int_{\mathcal{A}_{\Delta}(\mathbf{X}_k)} Nu(\mathbf{x}, t) d\mathbf{x} \quad (17)$$

i.e., as the spatial average of the local Nusselt number, defined in Eq. (3), over a square region $\mathcal{A}_{\Delta}(\mathbf{X}_k) = [X_k - \Delta/2, X_k + \Delta/2] \times [Z_k - \Delta/2, Z_k + \Delta/2]$ centered at position \mathbf{X}_k , with k running over the number of cells $[k = 1, \dots, (L/\Delta)^2]$. The cell size is fixed to $\Delta = L/28 = H/28 \approx 70$. It is chosen to represent the typical mesoscale of the system: small enough to resolve local features, but large enough to accommodate – on average – the size of a single droplet (based on the initialization diameter d) surrounded by a reasonable amount of continuous phase. The corresponding probability distribution functions (PDFs) of δNu_{mes} for both the stabilized and non-stabilized liquid-liquid dispersions are reported in Fig. 6 for some combinations of the (ϕ, Ra) pair. The Nu PDFs display the typical shape skewed towards positive values [70, 73, 118]; for lower values of Ra ,

no relevant mismatch is observed between the two kinds of dispersion, regardless of the value of ϕ . In contrast, at higher values of Ra , the PDF of the stabilized dispersion develops more pronounced tails in the more dilute case ($\phi = 0.17$), but, curiously, this mismatch is again suppressed as ϕ increases. This non-trivial behaviour prompted us to perform a more systematic study in the (ϕ, Ra) space, by investigating the standard deviation of the PDFs of δNu_{mes} , namely:

$$\sigma_{\text{mes}} = \sqrt{\langle (Nu_{\text{mes}} - \langle Nu_{\text{mes}} \rangle)^2 \rangle}. \quad (18)$$

The fluctuations σ_{mes} are reported in Fig. 7 as a function of Ra for two representative values of ϕ . In both cases, σ_{mes} grows with Ra , reflecting the expected rise in turbulence intensity. However, in the more diluted regime [see Fig. 7(a)], the fluctuations in the stabilized dispersion are systematically larger than those in the non-stabilized case, with the gap widening as Ra increases. A naive interpretation might link this trend to the total amount of interface area \bar{I} , which grows more steeply with Ra in the stabilized system [see Fig. 5(d)–(f)]. Yet this argument does not hold at higher volume fractions [Fig. 7(b)],

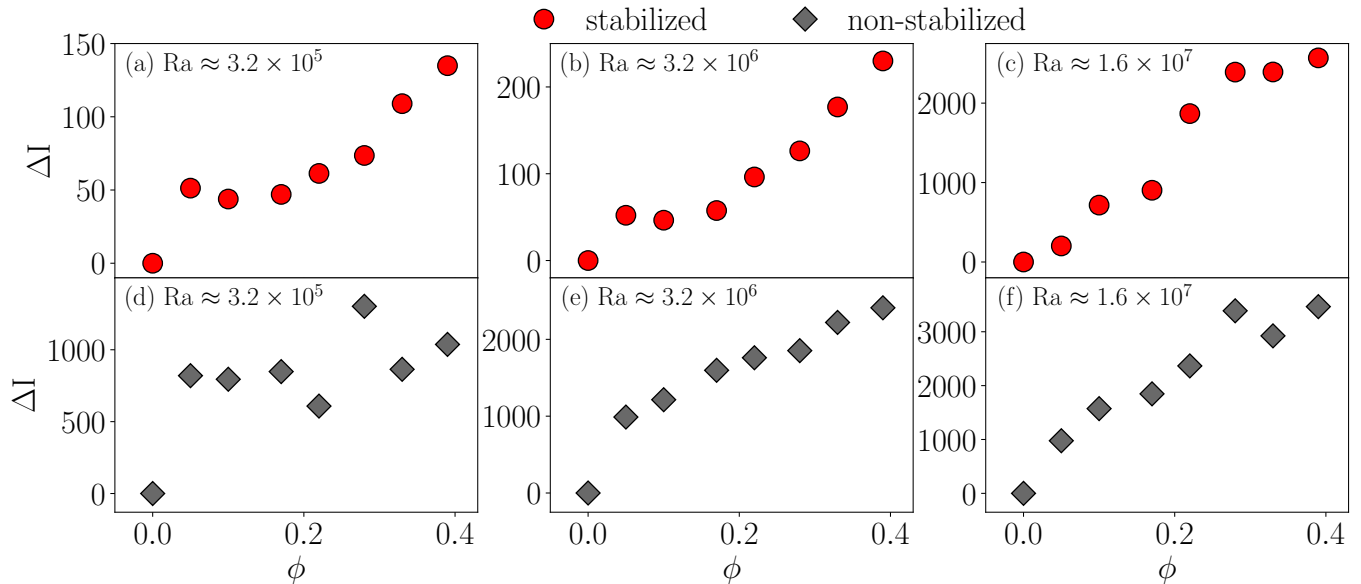


FIG. 10. Fluctuations of the interface indicator ΔI (see text for details), estimated from signals reported in Fig. 4, as a function of the volume fraction ϕ for different values of the Rayleigh number Ra . Data for both stabilized (red circles) and non-stabilized (grey diamonds) liquid-liquid dispersions are shown.

where the difference in σ_{mes} between the two systems becomes negligible, despite a further increase in interface area with ϕ . In Fig. 8 we also show the dependence of σ_{mes} on ϕ for $Ra = 1.6 \times 10^6$ [panel (a)] and $Ra = 1.6 \times 10^7$ [panel (b)]. We observe that, as the volume fraction ϕ increases, a clear separation gradually develops between the stabilized and non-stabilized dispersions, the latter consistently displaying higher values of σ_{mes} , which reflect in stronger mesoscale heat flux fluctuations. As ϕ increases and the dispersion becomes more concentrated, the gap eventually closes again, indicating that at high volume fractions the distinction between the two dispersions weakens. However, this gap does not arise from an increase in fluctuations in the stabilized dispersion. Indeed, two distinct trends can be identified. In the non-stabilized case, σ_{mes} initially decreases quite steadily and then remains constant for $\phi \gtrsim 0.2$, since droplet coalescence and restructuring suppress thermal transport. In the stabilized dispersion, σ_{mes} slowly decreases with ϕ . Overall, this entails a non-monotonic behaviour of the relative mismatch, as evidenced in Fig. 9, with a maximum around $0.1 < \phi < 0.2$ which weakly depends on Ra . A qualitative interpretation of the observed phenomenology relies on the link between heat flux fluctuations, quantified by σ_{mes} in Eq. (18), and the small-scale structure of the velocity field. In the absence of stabilization against coalescence, the non-stabilized liquid-liquid dispersion will develop domains of the dispersed phase across a range of length scales. These structures can interact with turbulent fluctuations, effectively “dissipating” kinetic energy through interface rearrangements such as coalescence and breakup. In contrast, in stabilized dispersion, where droplets remain relatively small

and resist merging, the interface dynamics becomes increasingly decoupled from the turbulent flow, particularly at low volume fractions, making the fluctuations σ_{mes} independent from ϕ . As Ra increases and the system becomes more concentrated, the frequency of droplet collisions rises, thereby enhancing the rate of coalescence. The latter promotes the formation of larger droplets, which are more prone to breakup, thus reactivating a dynamical balance between breakup and coalescence. This renewed interfacial activity draws energy from small-scale velocity fluctuations, which are consequently attenuated, resulting in a decrease of σ_{mes} with increasing ϕ . These facts are also supported by the study of fluctuations in the interface indicator, ΔI , which serves as a proxy for the number of breakup and coalescence events. Fig. 10 shows data of ΔI as a function of ϕ for different values of Ra . In non-stabilized liquid-liquid dispersions, the fluctuations ΔI continuously increase with ϕ ; contrariwise, for the stabilized case, ΔI is almost pinned up to $\phi \approx 0.2$ for any value of Ra , and then increases, a behaviour that is symptomatic of the resistance of the stabilized dispersion to morphological variations induced by the increase of collision/coalescence rate.

IV. CONCLUSIONS

We conducted a numerical investigation of the Raileigh-Bénard thermal convection in dispersions of liquid droplets in another liquid phase by comparing two different systems: a stabilized liquid-liquid dispersion (i.e., a proper emulsion), where a mechanism of interfacial stabilization against droplet coalescence is introduced

– mimicking the effect of surfactants via a positive disjoining pressure [1] – and a non-stabilized liquid-liquid dispersion, where the stabilization mechanism is not present. By systematically varying the droplet volume fraction ϕ and the Rayleigh number Ra , we explored both the system morphology and the heat transfer properties. Despite significant differences in the morphological evolution of the two systems, particularly in the interface indicator I , we find that the global heat transfer, quantified via the time-averaged Nusselt number \bar{Nu} , remains remarkably similar between stabilized and non-stabilized liquid-liquid dispersions across the explored parameter space. This result underscores the robustness of the macroscopic thermal transport properties, even in the presence of dramatically different interfacial physics, at least in the range of Ra explored. Our analysis further reveals that small-scale features are much more sensitive to the nature of the dispersion. In particular, the fluctuations of the mesoscale Nusselt number, δNu_{mes} , are systematically larger in stabilized dispersions, where droplet collisions and interface-mediated interactions sustain enhanced velocity and temperature gradients at the mesoscale. Conversely, in non-stabilized dispersions, coalescence leads to the suppression of small-scale fluctuations, especially at values of $\phi > 0.2$. Interestingly, the difference in mesoscale heat flux fluctuations between the two systems exhibits a non-monotonic behavior as a function of ϕ : it peaks around $0.1 < \phi < 0.2$ and diminishes at higher concentrations. This behavior can be understood in terms of the coupling between velocity fluctuations and interface dynamics at small scales, which differs between the two systems. These observations enrich the scenario described in our previous findings on the transition between breakup- and coalescence-dominated regimes

in proper emulsions [49], and are consistent with recent results at higher Ra highlighting fluctuation-driven heat transfer enhancement in non-stabilized liquid-liquid dispersions [47].

Overall, our results underscore the necessity of considering macroscopic observables in conjunction with other interfacial properties when analyzing the role of different interfacial properties in thermally convective multiphase systems. Despite global observables may appear insensitive to interfacial details, interfacial physics plays a critical role in shaping the small-scale structure and energy redistribution mechanisms of the flow. Future work will focus on further characterizing stabilized dispersions by studying systems with different strengths of the disjoining pressure in the interfacial interactions. This work will help clarify better how the phenomenology observed for stabilized dispersions sets in starting from a non-stabilized one. Additionally, extending the present analysis to three-dimensional systems could provide new insights into how dimensionality affects droplet dynamics and heat transport in thermally driven multiphase flows with complex interfacial properties.

ACKNOWLEDGEMENTS

The authors thank Chao Sun for fruitful discussions. FP, MS, and MB acknowledge the support of the National Center for HPC, Big Data and Quantum Computing, Project CN_00000013 – CUP E83C22003230001 and CUP B93C22000620006, Mission 4 Component 2 Investment 1.4, funded by the European Union – NextGenerationEU. Support from INFN/FIELDTURB project is also acknowledged.

-
- [1] F. Ravera, K. Dziza, E. Santini, L. Cristofolini, and L. Liggieri, Emulsification and emulsion stability: The role of the interfacial properties, *Advances in Colloid and Interface Science* **288**, 102344 (2021).
 - [2] S. Tcholakova, N. Denkov, and T. Danner, Role of surfactant type and concentration for the mean drop size during emulsification in turbulent flow, *Langmuir* **20**, 7444 (2004).
 - [3] H. A. Barnes, Rheology of emulsions—a review, *Colloids and Surfaces A: Physicochemical and Engineering Aspects* **91**, 89 (1994).
 - [4] T. Mason, New fundamental concepts in emulsion rheology, *Current Opinion in Colloid & Interface Science* **4**, 231 (1999).
 - [5] S. R. Derkach, Rheology of emulsions, *Advances in colloid and interface science* **151**, 1 (2009).
 - [6] T. F. Tadros, Emulsion formation, stability, and rheology, *Emulsion formation and stability* **1**, 1 (2013).
 - [7] R. Pal, Shear viscosity behavior of emulsions of two immiscible liquids, *Journal of colloid and interface science* **225**, 359 (2000).
 - [8] D. Bonn, M. M. Denn, L. Berthier, T. Divoux, and S. Manneville, Yield stress materials in soft condensed matter, *Reviews of Modern Physics* **89**, 035005 (2017).
 - [9] D. J. McClements, *Food emulsions: principles, practices, and techniques* (CRC press, 2015) p. 632.
 - [10] B. A. Khan, N. Akhtar, H. M. S. Khan, K. Waseem, T. Mahmood, A. Rasul, M. Iqbal, and H. Khan, Basics of pharmaceutical emulsions: A review, *African Journal of Pharmacy and Pharmacology* **5**, 2715 (2011).
 - [11] A. Davaille, P. Carrez, and P. Cordier, Fat plumes may reflect the complex rheology of the lower mantle, *Geophysical Research Letters* **45**, 1349 (2018).
 - [12] F. Goodarzi and S. Zendeheboudi, A comprehensive review on emulsions and emulsion stability in chemical and energy industries, *The Canadian Journal of Chemical Engineering* **97**, 281 (2019).
 - [13] E. Orowan, Convection in a non-newtonian mantle, continental drift, and mountain building, *Philosophical Transactions of the Royal Society A* **258**, 284 (1965).
 - [14] W. J. Morgan, Convection plumes in the lower mantle, *Nature* **230**, 42 (1971).

- [15] R. Montelli, G. Nolet, F. Dahlen, and G. Masters, A catalogue of deep mantle plumes: New results from finite-frequency tomography, *Geochemistry, Geophysics, Geosystems* **7** (2006).
- [16] S. French and B. Romanowicz, Broad plumes rooted at the base of the earth's mantle beneath major hotspots, *Nature* **525**, 95 (2015).
- [17] G. Marti-Mestres and F. Nielloud, Emulsions in health care applications—an overview, *Journal of Dispersion Science and Technology* **23**, 419 (2002).
- [18] M. M. Abdulredha, H. S. Aslina, and C. A. Luqman, Overview on petroleum emulsions, formation, influence and demulsification treatment techniques, *Arabian Journal of Chemistry* **13**, 3403 (2020).
- [19] L. Bai, S. Huan, O. J. Rojas, and D. J. McClements, Recent innovations in emulsion science and technology for food applications, *Journal of Agricultural and Food Chemistry* **69**, 8944 (2021).
- [20] M. Delgado, A. Lázaro, J. Mazo, and B. Zalba, Review on phase change material emulsions and microencapsulated phase change material slurries: Materials, heat transfer studies and applications, *Renewable and Sustainable Energy Reviews* **16**, 253 (2012).
- [21] F. Wang, W. Lin, Z. Ling, and X. Fang, A comprehensive review on phase change material emulsions: Fabrication, characteristics, and heat transfer performance, *Solar Energy Materials and Solar Cells* **191**, 218 (2019).
- [22] H. Bénard, Les tourbillons cellulaires dans une nappe liquide, *Journal de Physique Théorique et Appliquée* **11**, 1261 (1900).
- [23] L. Rayleigh, Lix. on convection currents in a horizontal layer of fluid, when the higher temperature is on the under side, *The London, Edinburgh, and Dublin Philosophical Magazine and Journal of Science* **32**, 529 (1916).
- [24] S. Chandrasekhar, *Hydrodynamic and hydromagnetic stability* (Oxford University Press, 1961).
- [25] C. Sun, Y.-H. Cheung, and K.-Q. Xia, Experimental studies of the viscous boundary layer properties in turbulent rayleigh-bénard convection, *Journal of Fluid Mechanics* **605**, 79 (2008).
- [26] K. Sugiyama, R. Ni, R. J. Stevens, T. S. Chan, S.-Q. Zhou, H.-D. Xi, C. Sun, S. Grossmann, K.-Q. Xia, and D. Lohse, Flow reversals in thermally driven turbulence, *Physical Review Letters* **105**, 034503 (2010).
- [27] G. Ahlers, S. Grossmann, and D. Lohse, Heat transfer and large scale dynamics in turbulent rayleigh-bénard convection, *Reviews of Modern Physics* **81**, 503 (2009).
- [28] D. Lohse and K.-Q. Xia, Small-scale properties of turbulent rayleigh-bénard convection, *Annual Review of Fluid Mechanics* **42**, 335 (2010).
- [29] F. Chillà and J. Schumacher, New perspectives in turbulent rayleigh-bénard convection, *The European Physical Journal E* **35**, 1 (2012).
- [30] J. D. Scheel, M. S. Emran, and J. Schumacher, Resolving the fine-scale structure in turbulent rayleigh-bénard convection, *New Journal of Physics* **15**, 113063 (2013).
- [31] R. E. Ecke and O. Shishkina, Turbulent rotating rayleigh-bénard convection, *Annual Review of Fluid Mechanics* **55**, 603 (2023).
- [32] Y. Zhang and Q. Zhou, Low-prandtl-number effects on global and local statistics in two-dimensional rayleigh-bénard convection, *Physics of Fluids* **36** (2024).
- [33] D. Lohse and O. Shishkina, Ultimate rayleigh-bénard turbulence, *Reviews of modern physics* **96**, 035001 (2024).
- [34] H. A. Stone, Dynamics of drop deformation and breakup in viscous fluids, *Annual Review of Fluid Mechanics* **26**, 65 (1994).
- [35] V. Cristini, S. Guido, A. Alfani, J. Bławdziewicz, and M. Loewenberg, Drop breakup and fragment size distribution in shear flow, *Journal of Rheology* **47**, 1283 (2003).
- [36] N. Vankova, S. Tcholakova, N. D. Denkov, I. B. Ivanov, V. D. Vulchev, and T. Danner, Emulsification in turbulent flow: 1. mean and maximum drop diameters in inertial and viscous regimes, *Journal of Colloid and Interface Science* **312**, 363 (2007).
- [37] N. Vankova, S. Tcholakova, N. Denkov, V. Vulchev, and T. Danner, Emulsification in turbulent flow: 2. breakage rate constants, *Journal of Colloid and Interface Science* **313**, 612 (2007).
- [38] S. Tcholakova, N. Vankova, N. Denkov, and T. Danner, Emulsification in turbulent flow: 3. daughter drop-size distribution, *Journal of Colloid and Interface Science* **310**, 570 (2007).
- [39] P. Perlekar, L. Biferale, M. Sbragaglia, S. Srivastava, and F. Toschi, Droplet size distribution in homogeneous isotropic turbulence, *Physics of Fluids* **24**, 065101 (2012).
- [40] L. Scarbolo, F. Bianco, and A. Soldati, Coalescence and breakup of large droplets in turbulent channel flow, *Physics of Fluids* **27** (2015).
- [41] A. Roccon, M. De Paoli, F. Zonta, and A. Soldati, Viscosity-modulated breakup and coalescence of large drops in bounded turbulence, *Physical Review Fluids* **2**, 083603 (2017).
- [42] G. Soligo, A. Roccon, and A. Soldati, Breakage, coalescence and size distribution of surfactant-laden droplets in turbulent flow, *Journal of Fluid Mechanics* **881**, 244 (2019).
- [43] H.-R. Liu, K. L. Chong, Q. Wang, C. S. Ng, R. Verzicco, and D. Lohse, Two-layer thermally driven turbulence: mechanisms for interface breakup, *Journal of Fluid Mechanics* **913**, A9 (2021).
- [44] I. Giroto, R. Benzi, G. Di Staso, A. Scagliarini, S. F. Schifano, and F. Toschi, Build up of yield stress fluids via chaotic emulsification, *Journal of Turbulence* **23**, 265 (2022).
- [45] I. Giroto, A. Scagliarini, R. Benzi, and F. Toschi, Lagrangian statistics of concentrated emulsions, *Journal of Fluid Mechanics* **986**, A33 (2024).
- [46] M. Cialesi-Esposito, G. Boffetta, L. Brandt, S. Chibbaro, and S. Musacchio, How small droplets form in turbulent multiphase flows, *Physical Review Fluids* **9**, L072301 (2024).
- [47] A. M. Bilondi, N. Scapin, L. Brandt, and P. Mirbod, Turbulent convection in emulsions: the rayleigh-bénard configuration, *Journal of Fluid Mechanics* **999**, A4 (2024).
- [48] F. Mangani, A. Roccon, F. Zonta, and A. Soldati, Heat transfer in drop-laden turbulence, *Journal of Fluid Mechanics* **978**, A12 (2024).
- [49] F. Pelusi, A. Scagliarini, M. Sbragaglia, M. Bernaschi, and R. Benzi, Dynamical regimes of thermally convective emulsions, *Physical Review E* **111**, 065401 (2025).

- [50] J. Zhang, D. Vola, and I. A. Frigaard, Yield stress effects on rayleigh–benard convection, *Journal of Fluid Mechanics* **566**, 389 (2006).
- [51] N. J. Balmforth and A. C. Rust, Weakly nonlinear viscoplastic convection, *Journal of Non-Newtonian Fluid Mechanics* **158**, 36 (2009).
- [52] A. Vikhansky, Thermal convection of a viscoplastic liquid with high rayleigh and bingham numbers, *Physics of Fluids* **21** (2009).
- [53] A. Vikhansky, On the onset of natural convection of bingham liquid in rectangular enclosures, *Journal of Non-Newtonian Fluid Mechanics* **165**, 1713 (2010).
- [54] B. Albaalbaki and R. E. Khayat, Pattern selection in the thermal convection of non-newtonian fluids, *Journal of Fluid Mechanics* **668**, 500 (2011).
- [55] N. J. Balmforth, I. A. Frigaard, and G. Ovarlez, Yielding to stress: Recent developments in viscoplastic fluid mechanics, *Annual Review of Fluid Mechanics* **46**, 121 (2014).
- [56] I. Karimfazli, I. Frigaard, and A. Wachs, Thermal plumes in viscoplastic fluids: flow onset and development, *Journal of Fluid Mechanics* **787**, 474 (2016).
- [57] M. S. Aghighi, C. Metivier, and S. Fakhri, Wall slip effects in rayleigh–bénard convection of viscoplastic materials, *Multidiscipline Modeling in Materials and Structures* **19**, 1275 (2023).
- [58] L. Plassard, A. Mouret, C. Nieto-Draghi, C. Dalmazzone, D. Langevin, and J.-F. Argillier, Comparison of methods used to investigate coalescence in emulsions, *Langmuir* **40**, 10847 (2024).
- [59] F. Bouchama, G. Van Aken, A. Autin, and G. Koper, On the mechanism of catastrophic phase inversion in emulsions, *Colloids and Surfaces A: Physicochemical and engineering aspects* **231**, 11 (2003).
- [60] A. Perazzo, V. Preziosi, and S. Guido, Phase inversion emulsification: Current understanding and applications, *Advances in Colloid and Interface Science* **222**, 581 (2015).
- [61] J. Weiss, C. Canceliere, and D. J. McClements, Mass transport phenomena in oil-in-water emulsions containing surfactant micelles: Ostwald ripening, *Langmuir* **16**, 6833 (2000).
- [62] Y.-T. Hu, Y. Ting, J.-Y. Hu, and S.-C. Hsieh, Techniques and methods to study functional characteristics of emulsion systems, *Journal of food and drug analysis* **25**, 16 (2017).
- [63] G. Urbina-Villalba, An algorithm for emulsion stability simulations: Account of flocculation, coalescence, surfactant adsorption and the process of ostwald ripening, *International Journal of Molecular Sciences* **10**, 761 (2009).
- [64] S. Aland, J. Lowengrub, and A. Voigt, Particles at fluid-fluid interfaces: A new navier-stokes-cahn-hilliard surface-phase-field-crystal model, *Physical Review E—Statistical, Nonlinear, and Soft Matter Physics* **86**, 046321 (2012).
- [65] O. Turan, N. Chakraborty, and R. J. Poole, Laminar rayleigh–bénard convection of yield stress fluids in a square enclosure, *Journal of Non-Newtonian Fluid Mechanics* **171–172**, 83 (2012).
- [66] A. Massmeyer, E. Di Giuseppe, A. Davaille, T. Rolf, and P. J. Tackley, Numerical simulation of thermal plumes in a herschel–bulkley fluid, *Journal of Non-Newtonian Fluid Mechanics* **195**, 32 (2013).
- [67] A. Gupta, M. Sbragaglia, and A. Scagliarini, Hybrid lattice boltzmann/finite difference simulations of viscoelastic multicomponent flows in confined geometries, *Journal of Computational Physics* **291**, 177 (2015).
- [68] M. Hassan, M. Pathak, and M. K. Khan, Rayleigh–benard convection in herschel–bulkley fluid, *Journal of Non-Newtonian Fluid Mechanics* **226**, 32 (2015).
- [69] M. E. Rosti, F. De Vita, and L. Brandt, Numerical simulations of emulsions in shear flows, *Acta Mechanica* **230**, 667 (2019).
- [70] F. Pelusi, M. Sbragaglia, R. Benzi, A. Scagliarini, M. Bernaschi, and S. Succi, Rayleigh–bénard convection of a model emulsion: anomalous heat-flux fluctuations and finite-size droplet effects, *Soft Matter* **17**, 3709 (2021).
- [71] F. Pelusi, D. Filippi, L. Derzsi, M. Pierno, and M. Sbragaglia, Emulsions in microfluidic channels with asymmetric boundary conditions and directional surface roughness: stress and rheology, *Soft Matter* (2024).
- [72] A. Tiribocchi, M. Durve, M. Lauricella, A. Montessori, J.-M. Tucny, and S. Succi, Lattice boltzmann simulations for soft flowing matter, *Physics Reports* **1105**, 1 (2025).
- [73] F. Pelusi, S. Ascione, M. Sbragaglia, and M. Bernaschi, Analysis of the heat transfer fluctuations in the rayleigh–bénard convection of concentrated emulsions with finite-size droplets, *Soft Matter* **19**, 7192 (2023).
- [74] P. Oresta, R. Verzicco, D. Lohse, and A. Prosperetti, Heat transfer mechanisms in bubbly rayleigh–bénard convection, *Physical Review E* **80**, 026304 (2009).
- [75] R. Lakkaraju, R. J. A. M. Stevens, P. Oresta, R. Verzicco, D. Lohse, and A. Prosperetti, Heat transport in bubbling turbulent convection, *Proceedings of the National Academy of Sciences* **110**, 9237 (2013).
- [76] L. Biferale, P. Perlekar, M. Sbragaglia, and F. Toschi, Convection in multiphase fluid flows using lattice boltzmann methods, *Physical Review Letters* **108**, 104502 (2012).
- [77] L. Biferale, P. Perlekar, M. Sbragaglia, and F. Toschi, Simulations of boiling systems using a lattice boltzmann method, *Communications in Computational Physics* **13**, 696 (2013).
- [78] H.-R. Liu, K. L. Chong, R. Yang, R. Verzicco, and D. Lohse, Heat transfer in turbulent rayleigh–bénard convection through two immiscible fluid layers, *Journal of Fluid Mechanics* **938**, A31 (2022).
- [79] H.-R. Liu, K. L. Chong, C. S. Ng, R. Verzicco, and D. Lohse, Enhancing heat transport in multiphase rayleigh–bénard turbulence by changing the plate–liquid contact angles, *Journal of Fluid Mechanics* **933**, R1 (2022).
- [80] P. R. Santos, A. Lugarini, S. L. Junqueira, and A. T. Franco, Natural convection of a viscoplastic fluid in an enclosure filled with solid obstacles, *International Journal of Thermal Sciences* **166**, 106991 (2021).
- [81] J. Goyon, A. Colin, G. Ovarlez, A. Ajdari, and L. Bocquet, Spatial cooperativity in soft glassy flows, *Nature* **454**, 84 (2008).
- [82] J. Goyon, A. Colin, G. Ovarlez, A. Ajdari, and L. Bocquet, How does a soft glassy material flow: finite size effects, non local rheology, and flow cooperativity, *Soft Matter* **6**, 2668 (2010).

- [83] A. Davaille, B. Gueslin, A. Massmeyer, and E. Di Giuseppe, Thermal instabilities in a yield stress fluid: existence and morphology, *Journal of Non-Newtonian Fluid Mechanics* **193**, 144 (2013).
- [84] F. Pelusi, A. Scagliarini, M. Sbragaglia, M. Bernaschi, and R. Benzi, Intermittent thermal convection in jammed emulsions, *Physical Review Letters* **133**, 244001 (2024).
- [85] G. Chen and D. Tao, An experimental study of stability of oil–water emulsion, *Fuel Processing Technology* **86**, 499 (2005).
- [86] A. Nesterenko, A. Drelich, H. Lu, D. Clausse, and I. Pezron, Influence of a mixed particle/surfactant emulsifier system on water-in-oil emulsion stability, *Colloids and Surfaces A: Physicochemical and Engineering Aspects* **457**, 49 (2014).
- [87] J.-L. Barrat, Elasticity and plasticity of disordered systems, a statistical physics perspective, *Physica A: Statistical Mechanics and its Applications* **504**, 20 (2017).
- [88] A. Nicolas, E. E. Ferrero, K. Martens, and J.-L. Barrat, Deformation and flow of amorphous solids: Insights from elastoplastic models, *Reviews of Modern Physics* **90**, 045006 (2018).
- [89] T. Divoux, E. Agoritsas, S. Aime, C. Barentin, J.-L. Barrat, R. Benzi, L. Berthier, D. Bi, G. Biroli, D. Bonn, *et al.*, Ductile-to-brittle transition and yielding in soft amorphous materials: perspectives and open questions, *Soft Matter* **20**, 6868 (2024).
- [90] S. Grossmann and D. Lohse, Thermal convection for large prandtl numbers, *Physical Review Letters* **86**, 3316 (2001).
- [91] F. Pelusi, M. Lulli, M. Sbragaglia, and M. Bernaschi, Tlbfind: a thermal lattice boltzmann code for concentrated emulsions with finite-size droplets, *Computer Physics Communications* **273**, 108259 (2022).
- [92] For all simulations, we fix $T_0 = 0$.
- [93] E. Bodenschatz, W. Pesch, and G. Ahlers, Recent developments in rayleigh-bénard convection, *Annual Review of Fluid Mechanics* **32**, 709 (2000).
- [94] For the values of Ra explored in this work, the Weber number is in the range $We \in [0.1, 40]$.
- [95] B. I. Shraiman and E. D. Siggia, Heat transport in high-rayleigh-number convection, *Physical Review A* **42**, 3650 (1990).
- [96] R. Stevens, R. Verzicco, and D. Lohse, Radial boundary layer structure and nusselt number in rayleigh-bénard convection, *Journal of Fluid Mechanics* **643**, 495 (2010).
- [97] R. Benzi, S. Succi, and M. Vergassola, The lattice boltzmann equation: theory and applications, *Physics Reports* **222**, 145 (1992).
- [98] T. Krüger, H. Kusumaatmaja, A. Kuzmin, O. Shardt, G. Silva, and E. M. Viggen, *The lattice boltzmann method*, Springer International Publishing **10**, 4 (2017).
- [99] S. Succi, *The lattice Boltzmann Equation* (Oxford University Press, 2018).
- [100] R. Benzi, M. Sbragaglia, P. Perlekar, M. Bernaschi, S. Succi, and F. Toschi, Direct evidence of plastic events and dynamic heterogeneities in soft-glasses, *Soft Matter* **10**, 4615 (2014).
- [101] B. Dollet, A. Scagliarini, and M. Sbragaglia, Two-dimensional plastic flow of foams and emulsions in a channel: experiments and lattice boltzmann simulations, *Journal of Fluid Mechanics* **766**, 556 (2015).
- [102] S. Leclaire, A. Parmigiani, O. Malaspinas, B. Chopard, and J. Latt, Generalized three-dimensional lattice boltzmann color-gradient method for immiscible two-phase pore-scale imbibition and drainage in porous media, *Physical Review E* **95**, 033306 (2017).
- [103] M. Lulli, R. Benzi, and M. Sbragaglia, Metastability at the yield-stress transition in soft glasses, *Physical Review X* **8**, 021031 (2018).
- [104] F. Pelusi, M. Sbragaglia, and R. Benzi, Avalanche statistics during coarsening dynamics, *Soft Matter* **15**, 4518 (2019).
- [105] F. Pelusi, M. Sbragaglia, A. Scagliarini, M. Lulli, M. Bernaschi, and S. Succi, On the impact of controlled wall roughness shape on the flow of a soft material, *EPL (Europhysics Letters)* **127**, 34005 (2019).
- [106] F. Pelusi, M. Segal, and J. Harting, Liquid film rupture beyond the thin-film equation: A multi-component lattice Boltzmann study, *Physics of Fluids* **34**, 062109 (2022).
- [107] The model employs a two dimensional D2Q9 lattice with 9 velocities \mathbf{c}_i indexed from $i = 0, \dots, 8$: $\mathbf{c}_0 = (0, 0)$, $\mathbf{c}_{1,3} = (\pm 1, 0)$, $\mathbf{c}_{2,4} = (0, \pm 1)$, $\mathbf{c}_{5,8} = (\pm 1, \pm 1)$, $\mathbf{c}_{6,7} = (-1, \pm 1)$.
- [108] The relaxation time is fixed to $\tau = 1$ in all simulations.
- [109] Weights w_i in the D2Q9 scheme: $w_0 = 4/9$, $w_{1,4} = 1/9$, $w_{5,8} = 1/36$.
- [110] X. Shan and H. Chen, Lattice boltzmann model for simulating flows with multiple phases and components, *Physical Review E* **47**, 1815 (1993).
- [111] M. Sbragaglia, R. Benzi, L. Biferale, S. Succi, K. Sugiyama, and F. Toschi, Generalized lattice boltzmann method with multirange pseudopotential, *Physical Review E* **75** (2007).
- [112] R. Benzi, M. Sbragaglia, S. Succi, M. Bernaschi, and S. Chibbaro, Mesoscopic lattice boltzmann modeling of soft-glassy systems: Theory and simulations, *Journal of Chemical Physics* **131**, 104903 (2009).
- [113] M. Sbragaglia, R. Benzi, M. Bernaschi, and S. Succi, The emergence of supramolecular forces from lattice kinetic models of non-ideal fluids: applications to the rheology of soft glassy materials, *Soft Matter* **8**, 10773 (2012).
- [114] We fix $\rho_0 = 0.83$.
- [115] E. A. Spiegel and G. Veronis, On the boussinesq approximation for a compressible fluid, *Astrophysical Journal* **131**, 442 (1960).
- [116] P. Perlekar, R. Benzi, H. J. Clercx, D. R. Nelson, and F. Toschi, Spinodal decomposition in homogeneous and isotropic turbulence, *Physical Review Letters* **112**, 014502 (2014).
- [117] F. Heslot, B. Castaing, and A. Libchaber, Transitions to turbulence in helium gas, *Physical Review A* **36**, 5870 (1987).
- [118] Y. Gasteuil, W. L. Shew, M. Gibert, F. Chilla, B. Castaing, and J.-F. Pinton, Lagrangian temperature, velocity, and local heat flux measurement in rayleigh-bénard convection, *Physical Review Letters* **99**, 234302 (2007).